

Seasonal and Interannual Variations of the Energy Flux Equator and ITCZ. Part II: Zonally Varying Shifts of the ITCZ

ORI ADAM

ETH Zürich, Zurich, Switzerland

TOBIAS BISCHOFF

California Institute of Technology, Pasadena, California

TAPIO SCHNEIDER

California Institute of Technology, Pasadena, California, and ETH Zürich, Zurich, Switzerland

(Manuscript received 6 October 2015, in final form 13 July 2016)

ABSTRACT

The ITCZ lies at the ascending branch of the tropical meridional overturning circulation, where near-surface meridional mass fluxes vanish. Near the ITCZ, column-integrated energy fluxes vanish, forming an atmospheric energy flux equator (EFE). This paper extends existing approximations relating the ITCZ position and EFE to the atmospheric energy budget by allowing for zonal variations. The resulting relations are tested using reanalysis data for 1979–2014. The zonally varying EFE is found as the latitude where the meridional component of the divergent atmospheric energy transport (AET) vanishes. A Taylor expansion of the AET around the equator relates the ITCZ position to derivatives of the AET. To a first order, the ITCZ position is proportional to the divergent AET across the equator; it is inversely proportional to the local atmospheric net energy input (NEI) that consists of the net energy fluxes at the surface, at the top of the atmosphere, and zonally across longitudes. The first-order approximation captures the seasonal migrations of the ITCZ in the African, Asian, and Atlantic sectors. In the eastern Pacific, a third-order approximation captures the bifurcation from single- to double-ITCZ states that occurs during boreal spring. In contrast to linear EFE theory, during boreal winter in the eastern Pacific, northward cross-equatorial AET goes along with an ITCZ north of the equator. EFE and ITCZ variations driven by ENSO are characterized by an equatorward (poleward) shift in the Pacific during El Niño (La Niña) episodes, which are associated with variations in equatorial ocean energy uptake.

1. Introduction

The intertropical convergence zone (ITCZ) is a band of deep convective clouds, located at the rising branch of the tropical meridional overturning (Hadley) circulation (Fig. 1), where near-surface meridional mass fluxes vanish. Since the Hadley circulation transports energy away from the ITCZ and dominates the tropical energy transport, column-integrated energy fluxes also vanish and diverge near the ITCZ, forming an atmospheric energy flux equator (EFE) (e.g., Neelin and Held 1987;

Broccoli et al. 2006; Kang et al. 2008, 2009; Donohoe et al. 2013, 2014; Adam et al. 2016).

The approximate collocation of the ITCZ and EFE provides a basis for relating the mean ITCZ position to the atmospheric energy transport (AET). Usually, an ITCZ and EFE north of the equator imply southward AET across the equator, away from the ITCZ, and vice versa. Indeed, the zonal-mean position of the ITCZ was found to be closely related to cross-equatorial AET in observations (e.g., Donohoe et al. 2013, 2014; Adam et al. 2016) and in climate models of varying complexity (e.g., Chiang and Bitz 2005; Broccoli et al. 2006; Yoshimori and Broccoli 2008; Kang et al. 2008, 2009; Donohoe et al. 2013, 2014).

Relating the ITCZ and EFE to the AET provides theoretical insight into, for example, the ocean's role in

Corresponding author address: Ori Adam, Department of Earth Sciences, ETH Zürich, Sonneggstrasse 5, 8092 Zurich, Switzerland.
E-mail: ori.adam@live.com

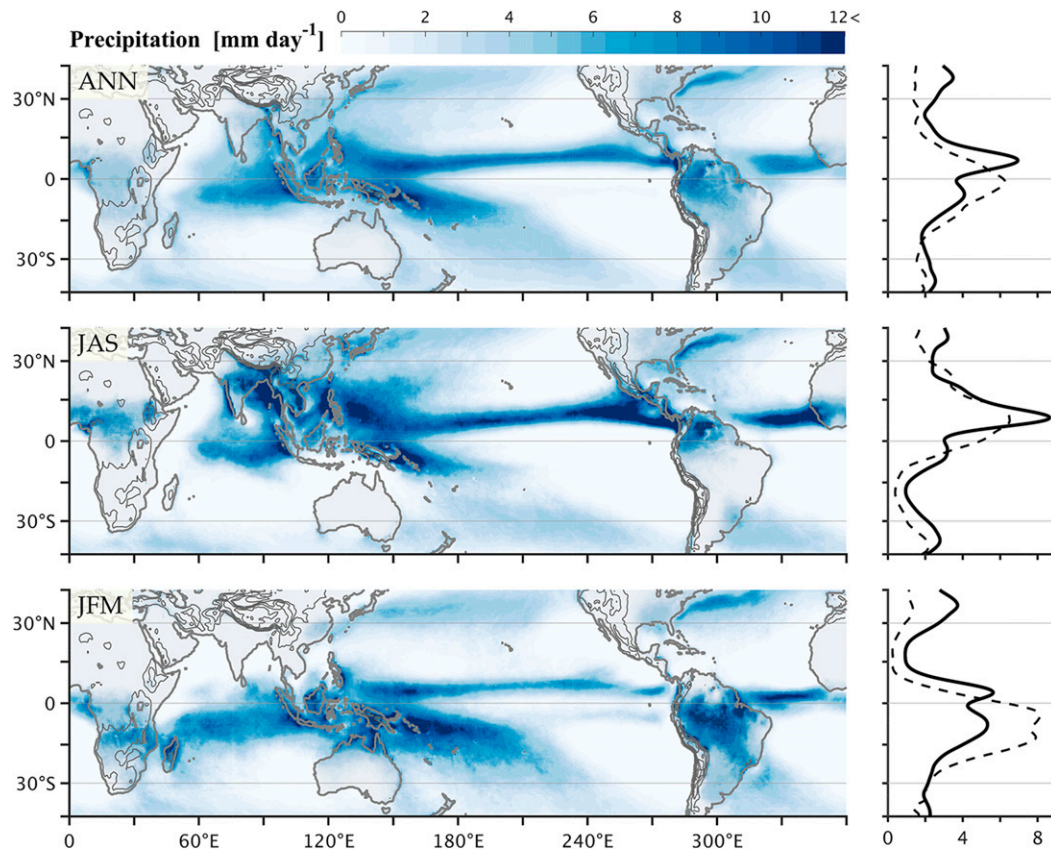


FIG. 1. (left) Mean precipitation (mm day^{-1}) for (top) ANN, (middle) boreal summer (JAS), and (bottom) boreal winter (JFM). Orography is shown by gray contours at 1-km intervals. (right) The respective zonal-mean precipitation over ocean (solid) and land (dashed). Data are from the Tropical Rainfall Measuring Mission Multisatellite Precipitation Analysis (Liu et al. 2012) for 1998–2014.

setting the mean position of the ITCZ (Frierson et al. 2013; Marshall et al. 2014), the effect of extratropical forcing on the mean ITCZ position (e.g., Chiang and Bitz 2005; Broccoli et al. 2006; Yoshimori and Broccoli 2008; Kang et al. 2008; Frierson and Hwang 2012; Bischoff and Schneider 2014), and the mean ITCZ position in past climates (Donohoe et al. 2013; Schneider et al. 2014). Such studies have quantitatively related the ITCZ position to the atmospheric energy budget in the zonal mean, but they have made only qualitative inferences about zonal variations of the ITCZ position, if at all [see Chiang and Friedman (2012) and Schneider et al. (2014) for reviews].

Here we extend previous results to zonal variations of the ITCZ position, which are a central characteristic of the tropical hydrological cycle (Fig. 1). For example, seasonal meridional migrations of marine ITCZs are small relative to their continental (monsoonal) counterparts (Fig. 1); interannual variations of the ITCZ associated with ENSO are most pronounced over the Pacific but are relatively small elsewhere (e.g., Dai and Wigley 2000; Adam et al. 2016); and the eastern Pacific

ITCZ bifurcates to a double ITCZ that straddles the equator during boreal spring, but such bifurcations do not usually occur elsewhere (Fig. 1, bottom; Zhang 2001; Gu et al. 2005). We will examine the extent to which energetic arguments can be extended to account for such zonally varying shifts of the ITCZ.

Using reanalysis data, we have recently shown that the zonal-mean EFE and ITCZ position covary on seasonal and interannual time scales and that seasonal and interannual variations of the ITCZ position can be quantitatively related to variations of the AET and its derivatives (Adam et al. 2016). In the present paper, we examine the relation between the zonally varying EFE and ITCZ and extend the theoretical framework developed for zonal-mean variations (Bischoff and Schneider 2014, 2016; Schneider et al. 2014; Adam et al. 2016) to regional variations. Using reanalysis data, we focus on the ITCZ in separate zonal sectors, to account for such observed features as the eastern Pacific double-ITCZ bifurcation in boreal spring, and local ITCZ shifts associated with ENSO.

The data and methods employed are described in section 2. Some theoretical aspects of the zonally varying EFE are derived in section 3. The data analysis is presented in section 4, followed by a summary and discussion in section 5.

2. Data and methods

The analysis uses four-times-daily data from the European Centre for Medium-Range Weather Forecasts (ECMWF) interim reanalysis (ERA-Interim, hereinafter ERAI; Dee et al. 2011) for 1979–2014. As in Adam et al. (2016), column-integrated fluxes are adjusted using a barotropic mass-flux correction (Trenberth 1997; see <http://www.cgd.ucar.edu/cas/catalog/newbudgets/> for detailed documentation). The fluxes are calculated from pressure level ERAI data; they agree well with fluxes calculated using native ERAI model grids (Fasullo and Trenberth 2008). We also used the oceanic Niño index (ONI) obtained from version 3b of the Extended Reconstructed Sea Surface Temperature (ERSST.v3b) dataset, provided by NOAA's National Climatic Data Center (Smith et al. 2008). For data retrieval and analysis we used the geophysical observation analysis tool (GOAT), a free MATLAB-based tool for geophysical data management (<http://www.goat-geo.org>).

Following Adam et al. (2016), the ITCZ position is defined as the latitude of maximal tropical precipitation, which we found to be more consistent with zonal-mean EFE variations than other ITCZ position indices [see Adam et al. (2016) for a discussion of other ITCZ position indices]. To reduce grid dependence, the zonally varying ITCZ position ϕ_{\max} is calculated as an expected latitude, weighted by the 10th power of the area-weighted precipitation P , integrated between the latitudes 20°S and 20°N:

$$\phi_{\max} = \frac{\int_{20^{\circ}\text{S}}^{20^{\circ}\text{N}} \phi [\cos(\phi)P]^{10} d\phi}{\int_{20^{\circ}\text{S}}^{20^{\circ}\text{N}} [\cos(\phi)P]^{10} d\phi}. \quad (1)$$

The 10th power was found to reliably identify the precipitation maximum, while smoothing grid-discretization noise.

3. Theory

Here we briefly review and extend the first- and third-order approximations, described in Bischoff and Schneider (2014, 2016), for a zonally varying EFE. See Schneider et al. (2014) for a review of the underlying concepts.

a. First-order approximation

The column-integrated energy balance of the atmosphere can be written as follows (Peixoto and Oort 1992; Adam et al. 2016):

$$\partial_t \langle e \rangle + \nabla \cdot \langle \mathbf{u}h \rangle = I + \varepsilon. \quad (2)$$

On the lhs, angle brackets denote the mass-weighted column integral, e denotes moist enthalpy, h denotes moist static energy (MSE), t denotes time, and $\mathbf{u} = (u, v, w)$ is the three-dimensional wind vector. The rhs is the atmospheric net energy input (NEI), where I denotes the difference between top-of-the-atmosphere (TOA) net radiative energy input and surface energy uptake (associated primarily with ocean heat storage or transport) and ε denotes residuals associated with either uncertainty in the column-integrated fluxes or computational error (e.g., in the calculation of the mass-flux adjustment). However, because of uncertainties in the radiative energy budget of the ERAI dataset (Trenberth et al. 2001), we calculated NEI as the rhs of Eq. (2) using the mass-flux corrected fluxes on the lhs.

Since deep convection involves strong vertical motions, tropical precipitation is closely linked to horizontal divergence of mass and energy fluxes. Therefore, the divergent component of the AET can often be related to the ITCZ. Since MSE typically increases with altitude, AET generally diverges where mean vertical motions in the tropics are upward (Yu et al. 1998)—potentially with the exception of a narrow region in the mid-Pacific (Back and Bretherton 2006). We therefore define the zonally varying EFE as the latitude where the meridional component of the divergent column-integrated MSE flux both vanishes and has a positive meridional gradient. The divergent fluxes (denoted by $\langle \cdot \rangle^\dagger$) are calculated as

$$\langle \mathbf{u}h \rangle^\dagger = \nabla \chi, \quad (3a)$$

where the potential χ is defined as

$$\chi = \nabla^{-2}(\nabla \cdot \langle \mathbf{u}h \rangle). \quad (3b)$$

Since the divergence of the rotational component of the energy flux is identically zero, the energy balance in Eq. (2) can be rearranged as follows:

$$\partial_y \langle v h \rangle^\dagger + \nabla \cdot \langle \mathbf{u}h \rangle - \partial_x \langle u h \rangle^\dagger = I^* - \partial_t \langle e \rangle + \varepsilon, \quad (4)$$

where $I^* = I - \partial_x \langle u h \rangle^\dagger$ denotes local NEI, composed of the net of vertical fluxes I across the top of the atmosphere and the surface and zonal fluxes $-\partial_x \langle u h \rangle^\dagger$ across

boundaries of atmospheric columns. For simplicity, Cartesian notation is used, but all calculations are performed in spherical coordinates.

By meridionally expanding the energy flux at the equator to the first order, assuming it vanishes at the ITCZ at latitude ϕ_I , and using the energy balance in the form of Eq. (4), we obtain the following:

$$\tilde{\phi}_I = -\frac{1}{a} \frac{\langle vh \rangle_0^\dagger}{\partial_y \langle vh \rangle_0^\dagger} = -\frac{1}{a} \frac{\langle vh \rangle_0^\dagger}{I_0^* - \partial_I \langle e \rangle_0 + \varepsilon_0}, \quad (5a)$$

where $(\cdot)_0$ denotes an average near the equator (in practice, an average between 5°S and 5°N). Neglecting ε_0 and energy storage, the stationary ITCZ position is given by

$$\phi_I = -\frac{1}{a} \frac{\langle vh \rangle_0^\dagger}{I_0^*}. \quad (5b)$$

Averaging the energy balance in Eq. (4) over a zonal sector, the storage-dependent and stationary sector-mean solutions are the following:

$$[\tilde{\phi}_I]_{\lambda_1}^{\lambda_2} = -\frac{1}{a} \frac{\langle [vh]_{\lambda_1}^{\lambda_2} \rangle_0^\dagger}{\partial_y \langle [vh]_{\lambda_1}^{\lambda_2} \rangle_0^\dagger} \quad (6a)$$

and

$$[\phi_I]_{\lambda_1}^{\lambda_2} = -\frac{1}{a} \frac{\langle [vh]_{\lambda_1}^{\lambda_2} \rangle_0^\dagger}{[I_0^*]_{\lambda_1}^{\lambda_2}} = -\frac{1}{a} \frac{\langle [vh]_{\lambda_1}^{\lambda_2} \rangle_0^\dagger}{[I_0^*]_{\lambda_1}^{\lambda_2} - \frac{1}{\lambda_2 - \lambda_1} \langle uh \rangle_0^\dagger \Big|_{\lambda_1}^{\lambda_2}}, \quad (6b)$$

where $[\cdot]_{\lambda_1}^{\lambda_2}$ denotes the zonal mean over a sector delimited by longitudes λ_1 and λ_2 . Since the zonal mean of the rotational component of the meridional energy flux and $\partial_x \langle uh \rangle_0^\dagger$ are both identically zero, setting $(\lambda_1, \lambda_2) = [0, 2\pi]$ in Eq. (6) reproduces the zonal-mean first-order approximation (Bischoff and Schneider 2014; Schneider et al. 2014; Adam et al. 2016). Thus, to a first order, the zonally varying position of the ITCZ is proportional to the meridional component of the divergent cross-equatorial AET and inversely proportional to the local NEI at the equator in the longitude sector in question.

b. Third-order approximation

A single ITCZ (and therefore single EFE) is associated with the rising branch of a tropical meridional overturning circulation transporting energy away from the ITCZ (Fig. 2a). Thus, since the

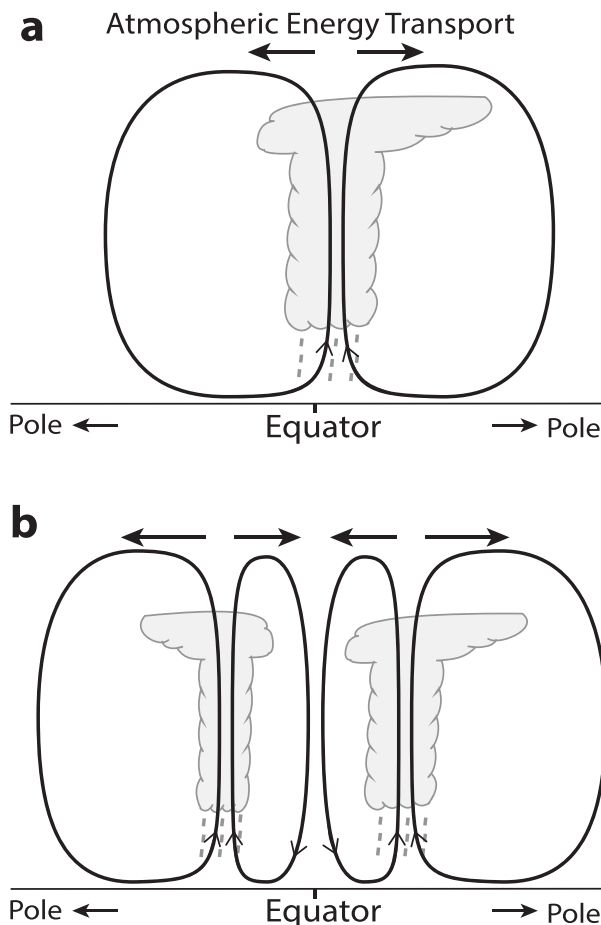


FIG. 2. Sketch of the meridional overturning circulation and column-integrated meridional atmospheric energy transport in (a) single-ITCZ and (b) double-ITCZ states.

column-integrated AET is positive north of the ITCZ and negative south of the ITCZ, the meridional gradient of the AET (i.e., approximately the local NEI) near a single ITCZ is positive. Conversely, negative local NEI near the equator corresponds to convergence of energy. Since eddy energy transport is weak near the equator, transport of energy toward the equator is done by the mean circulation. Therefore, for sufficiently strong convergence near the equator, the meridional overturning circulation adjusts to two meridional overturning cells straddling the equator and transporting energy toward their shared descending branch (Fig. 2b; Bischoff and Schneider 2016). In such states, precipitation is inhibited in the equatorial descending branch; precipitation occurs at the rising branches of these cells on either side of the equator. Thus, strong convergence of AET near the equator can be associated with a double-ITCZ state.

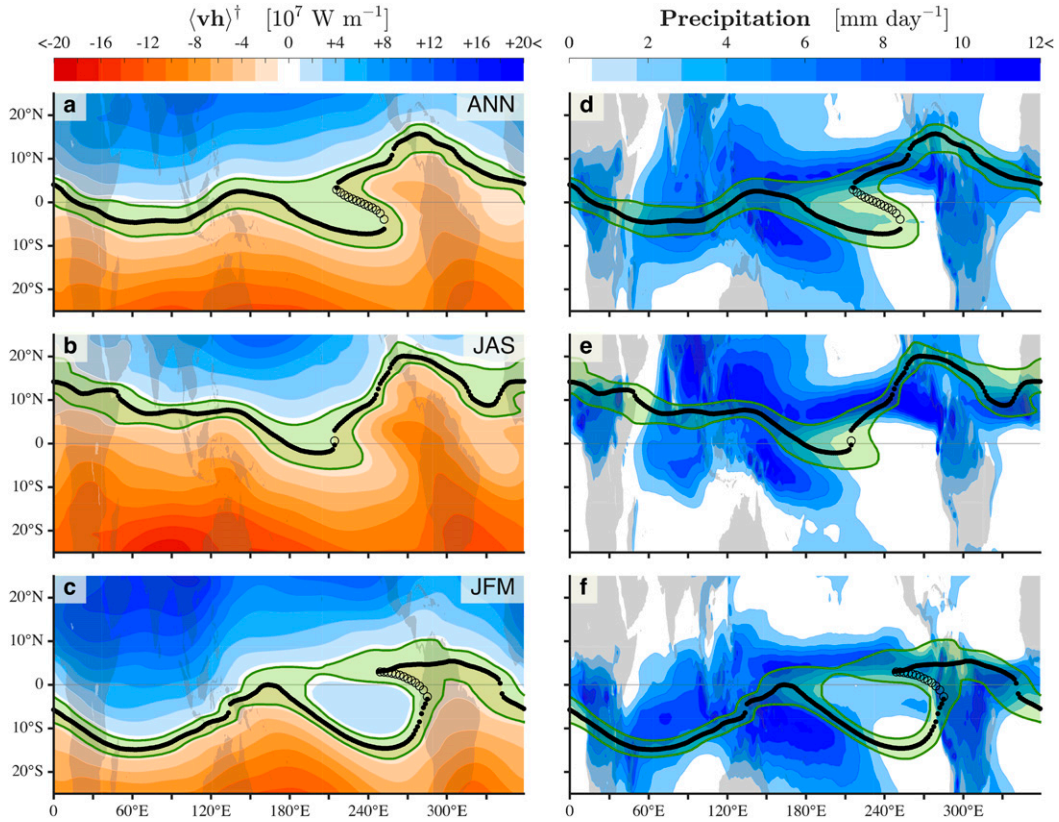


FIG. 3. ANN, JAS, and JFM averages of the meridional component of the (a)–(c) divergent MSE flux $\langle v h \rangle^\dagger$ and (d)–(f) precipitation. Precipitation and $\langle v h \rangle^\dagger$ are zonally smoothed using a running mean with a scale of 2500 km. The EFE (divergent zeros of $\langle v h \rangle^\dagger$) is shown with black dots. Convergent $\langle v h \rangle^\dagger$ zeros (implying a descending branch) are shown with open circles. The same error margin (shaded green, indicating regions where $|\langle v h \rangle_0^\dagger| < 1.4 \times 10^7 \text{ W m}^{-1}$) is used in all seasons. Data are from ERAI for 1979–2014.

However, double-ITCZ states (i.e., precipitation peaks that straddle the equator) can exist without convergence of energy near the equator (e.g., Voigt and Shaw 2015). Moreover, in the western Pacific and over the Indian Ocean during JAS (Fig. 1), precipitation peaks exist on both sides of the equator even though there is no AET convergence in these regions (Fig. 3). The double-ITCZ state shown in Fig. 2b therefore represents an extreme case in which the bifurcation from single- to double-ITCZ states is associated with negative NEI. In less extreme cases, small positive NEI near the equator may suffice to produce local precipitation maxima straddling the equator.

For nonlinear AET near the equator, a third-order (or higher order) expansion of the AET is required to account for the ITCZ position (Bischoff and Schneider 2016). The third-order solutions can be simplified by utilizing the antisymmetric nature of AET about the equator (see next section), rendering the meridional second derivative of the AET weak near the equator (Bischoff and Schneider 2016). An approximate discriminant

of the third-order polynomial can then be written as follows:

$$\Delta_I \equiv I_0^* + \sqrt[3]{\left(\langle v h \rangle_0^\dagger\right)^2 \partial_{yy} I_0^*}. \quad (7)$$

For $\Delta_I > 0$, the polynomial has one real root (e.g., Irving 2004), corresponding to a single ITCZ. In this case, the third- and zeroth-order terms approximately balance, and the single-ITCZ position is approximately given by

$$\phi_I = \frac{1}{a} \sqrt[3]{\frac{-6\langle v h \rangle_0^\dagger}{\partial_{yy} I_0^*}}. \quad (8a)$$

For $\Delta_I < 0$, the polynomial has three distinct real roots (e.g., Irving 2004), corresponding to a double-ITCZ state (with two roots corresponding to the ITCZs and one root to the divider between the deep tropical cells; see Fig. 2b). Using a first-order asymptotic expansion in $\langle v h \rangle_0^\dagger$ (see appendix), the ITCZ positions are thus approximately given by

$$\phi_I = -\frac{3}{2a} \frac{\partial_y I_0^*}{\partial_{yy} I_0^*} \pm \frac{1}{a} \sqrt{\frac{-6I_0^*}{\partial_{yy} I_0^*}} + \frac{\langle v h \rangle_0^\dagger}{a} \left[2I_0^* + \frac{\partial_y I_0^*}{2} \left(-\frac{3}{2} \frac{\partial_y I_0^*}{\partial_{yy} I_0^*} \pm \sqrt{\frac{-6I_0^*}{\partial_{yy} I_0^*}} \right) \right]^{-1}. \quad (8b)$$

For completeness, second-order terms are not neglected here but are assumed to be small. In what follows, we will examine the applicability of these solutions.

4. Results

a. Zonally varying EFE and ITCZ

Figure 3 shows the annual (ANN), July–September (JAS), and January–March (JFM) averages of the meridional component of the divergent MSE flux $\langle v h \rangle^\dagger$ (Fig. 3a–c), and precipitation (Fig. 3d–f). The zonally varying EFEs (zeros of $\langle v h \rangle^\dagger$, where $\partial_y \langle v h \rangle^\dagger > 0$) are shown with black dots. Open circles are shown where the meridional AET vanishes but is convergent (i.e., zeros of $\langle v h \rangle^\dagger$, where $\partial_y \langle v h \rangle^\dagger < 0$), implying a descending branch.

As an error margin of the EFE, we use one standard deviation of the differences between annually averaged $\langle v h \rangle^\dagger$ calculated directly from the MSE flux divergence [Eq. (3b)] and from NEI calculated as the sum of top of the atmosphere radiative fluxes and surface radiative and heat fluxes [i.e., assuming $\partial_y \langle e \rangle$ and $\varepsilon = 0$ in Eq. (2)]. The error margin (shaded green) of the zeros therefore reflects uncertainty in the reanalysis data.

As seen in previous studies (e.g., Chiang and Friedman 2012), the EFE migrates seasonally toward the differentially warming hemisphere (Fig. 3). It captures some aspects of the regional seasonal migration of the ITCZ. Over the Pacific, the divergent circulation is not predominantly meridional, offsetting the location of the EFE relative to the ITCZ. During boreal winter (Figs. 3c,f), the EFE splits into a North Pacific branch, which follows the North Pacific ITCZ, and a South Pacific branch, which deviates from the precipitation maximum. Discrepancies between the zonally varying EFE and ITCZ position exist either where column-integrated energy and mass fluxes do not simultaneously vanish or where the circulation is not primarily meridional. The large discrepancies observed in Fig. 3 indicate that the EFE framework is inapplicable at small regional scales, especially in the central and western Pacific.

b. Sector-mean EFE

Since the meridional derivative of $\langle v h \rangle^\dagger$ is generally positive in the tropics away from the equator (Fig. 3), the

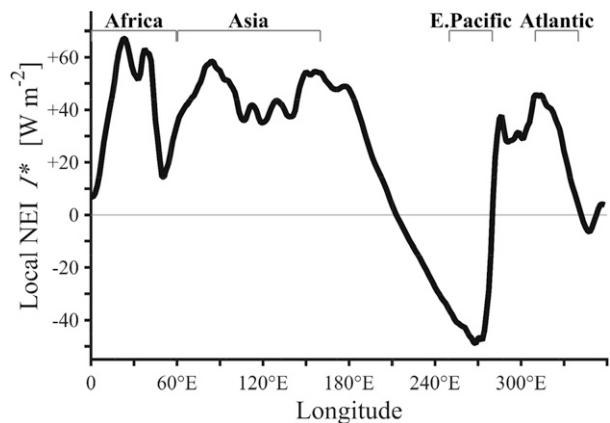


FIG. 4. Longitudinal dependence of the annual-mean local net energy input I_0^* (meridionally averaged between 5°S and 5°N). Data are from ERAI for 1979–2014.

condition for invoking third-order solutions is that the meridional derivative of $\langle v h \rangle^\dagger$ near the equator (i.e., approximately local NEI I_0^*) is small or negative. The annual-mean I_0^* as a function of longitude is shown in Fig. 4. The negative values of I_0^* in the Pacific indicate that in this sector, where both ITCZ and EFE bifurcate (Fig. 3), the third-order approximation is required. We therefore apply the first-order approximation [Eq. (6)] to the African (0°–60°E), Asian (60°–160°E), and Atlantic (310°–340°E) sectors and the third-order approximation [Eq. (8)] to the eastern Pacific (250°–280°E) sector. Since the circulation is not primarily meridional near the rising branch of the Walker circulation, we exclude the western Pacific sector from the analysis. In addition, frequent bifurcations from single- to double-ITCZ states occur during boreal spring in the central Pacific (Haffke et al. 2016). Conditional averaging of daily precipitation would therefore be required for a quantitative analysis there. We therefore also exclude the central Pacific from the present analysis, which focuses on seasonal and interannual variations.

Figure 5 shows the daily sector-mean climatology of the EFE (black) and its first-order approximations (red), on top of precipitation, for the African (Fig. 5a), Asian (Fig. 5d), and Atlantic (Fig. 5g) sectors. The respective cross-equatorial fluxes and NEI are shown in the line plots in Fig. 5. To remove regional subseasonal variability, sector means are smoothed using a 3-month running mean. [The EFE framework is not applicable on subseasonal time scales because tropical overturning and radiative relaxation times are on the order of several weeks (Adam et al. 2016).] However, the results do not qualitatively change if a 1-month running mean is used, as in Donohoe et al. (2014) and Adam et al. (2016) for the zonal-mean EFE. Equatorial means of the cross-equatorial

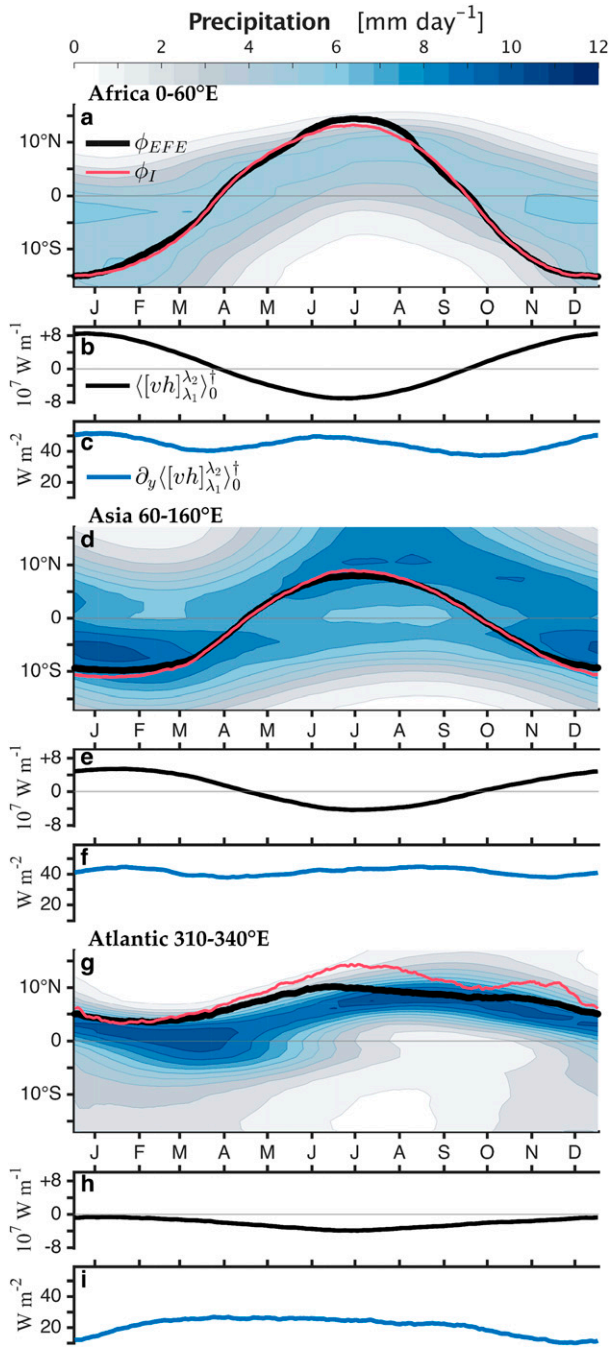


FIG. 5. (a),(d),(g) Daily climatology of zonal-mean precipitation (colors) in the African, Asian, and Atlantic sectors. The EFE latitude ϕ_{EFE} is shown by the thick black line. The stationary first-order approximation [Eq. (6b)] is shown in red. (b),(e),(h) Cross-equatorial AET $\langle [vh]_{\lambda_1}^{\lambda_2} \rangle_0^\dagger$ for each sector. (c),(f),(i) Equatorial atmospheric NEI $[I_{0,\lambda_1}^{\lambda_2}]_0^\dagger$ for each sector. Cross-equatorial AET and near-equator derivatives are meridionally averaged between 5°S and 5°N . Data are taken from ERAI for 1979–2014 and are smoothed using a 91-day running mean.

fluxes and all derivatives are averaged between 5°S and 5°N . The first-order approximations [Eq. (6)] are insensitive to the choice of near-equatorial averages (Adam et al. 2016). However, the third-order approximate solutions [Eq. (8)] deviate if the near-equatorial averages are extended beyond 5° .

The correlation between EFE and ITCZ position [Eq. (1)] variations in these sectors is maximal ($R > 0.9$) for precipitation that lags EFE variations by about 1 month. However, even when accounting for the lag between EFE and ITCZ variations, the EFE deviates from the ITCZ position by up to 5° . In the African and Asian sectors, the stationary first-order approximation [Eq. (6b)] is in near-perfect agreement with the EFE, indicating that a linear approximation is sufficient in these sectors. However, over the Atlantic, the stationary approximation [Eq. (6b)] deviates by several degrees from the EFE during boreal summer and autumn. By explicitly calculating the energy storage term in Eq. (5a), we find that the difference between the approximations in Eqs. (6a) and (6b) is negligible in all three sectors, indicating that near-equatorial energy storage can be neglected. The deviation of the solution in Eq. (6b) from the EFE in the Atlantic sector therefore results from the inadequacy of the first-order approximation.

In the three sectors, seasonal EFE variations are driven by variations in both cross-equatorial AET and equatorial NEI. Seasonal variations in NEI contribute roughly 25% to the EFE variations over Africa, 20% over Asia, and 100% over the Atlantic. Moreover, variations in cross-equatorial AET and equatorial NEI differ substantially between sectors. For example, $\langle [vh] \rangle^\dagger$ is southward year-round in the Atlantic sector but changes sign elsewhere (Fig. 3). The annual-mean equatorial NEI in this sector is relatively low (18 W m^{-2} compared with 42 and 46 W m^{-2} in the African and Asian sectors, respectively), accounting for the greater sensitivity of the EFE to variations in NEI.

The relation of precipitation, AET, and the 500-hPa vertical wind in the eastern Pacific ($250^\circ\text{--}280^\circ\text{E}$) is shown in Fig. 6 for December–January, March–April, June–July, and September–October (Figs. 6a–d, respectively). The nonlinearity of AET near the equator in the eastern Pacific (Fig. 4) persists year-round. In addition, because of the antisymmetry of the AET near the equator, second-order terms in the expansion of the AET around the equator are small (less than 10%) relative to the third-order terms, justifying the approximation used to derive Eqs. (7) and (8). Consistent with Eq. (7), the bifurcation from one to three AET roots occurs for small $\langle [vh] \rangle_0^\dagger$ and negative local NEI (i.e., for $\Delta_I < 0$). However, during December–January an ITCZ does not form at the southern AET zero; the bifurcation

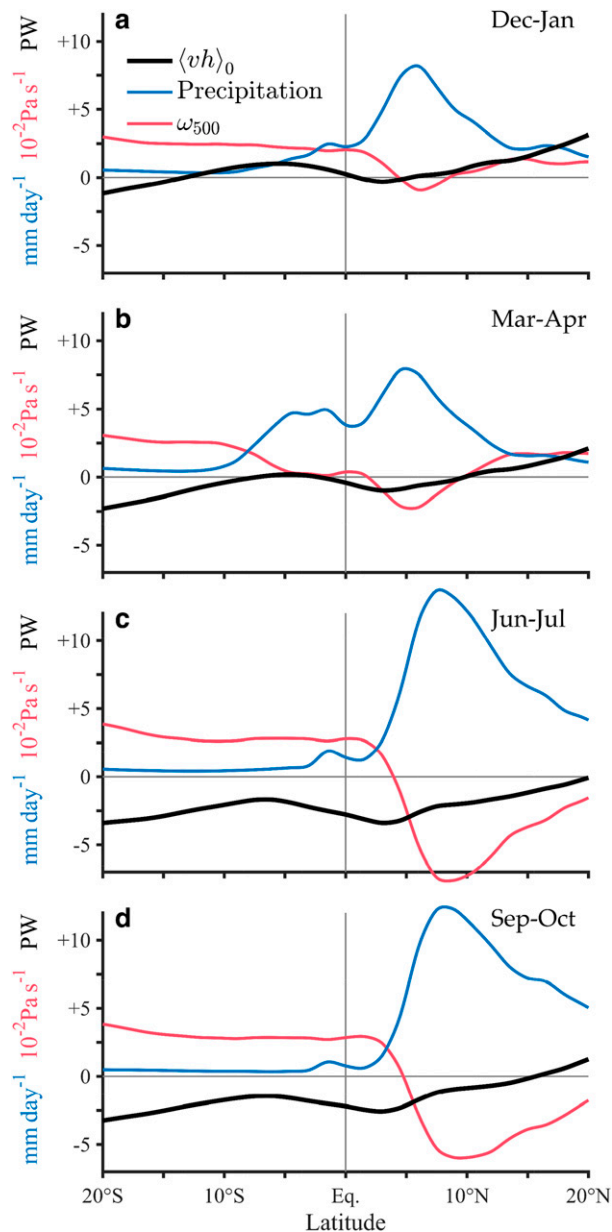


FIG. 6. Eastern Pacific (250°–280°E) divergent component of the meridional AET $\langle [vh]_{\lambda_1}^{\lambda_2} \rangle_0^{\dagger}$ (black), precipitation (blue), and vertical wind at the 500-hPa level (red), during the climatological mean (a) December–January, (b) March–April, (c) June–July, and (d) September–October. Data are taken from ERAI for 1979–2014 and are smoothed using a 91-day running mean.

from a single- to double-ITCZ occurs only during March–April (Fig. 6). Moreover, during December–January, the ITCZ is north of the equator even though cross-equatorial AET is positive. This demonstrates that contrary to linear EFE theory (e.g., Kang et al. 2008, 2009; Donohoe et al. 2013, 2014), for negative equatorial NEI, the ITCZ latitude and cross-equatorial AET can have the same sign.

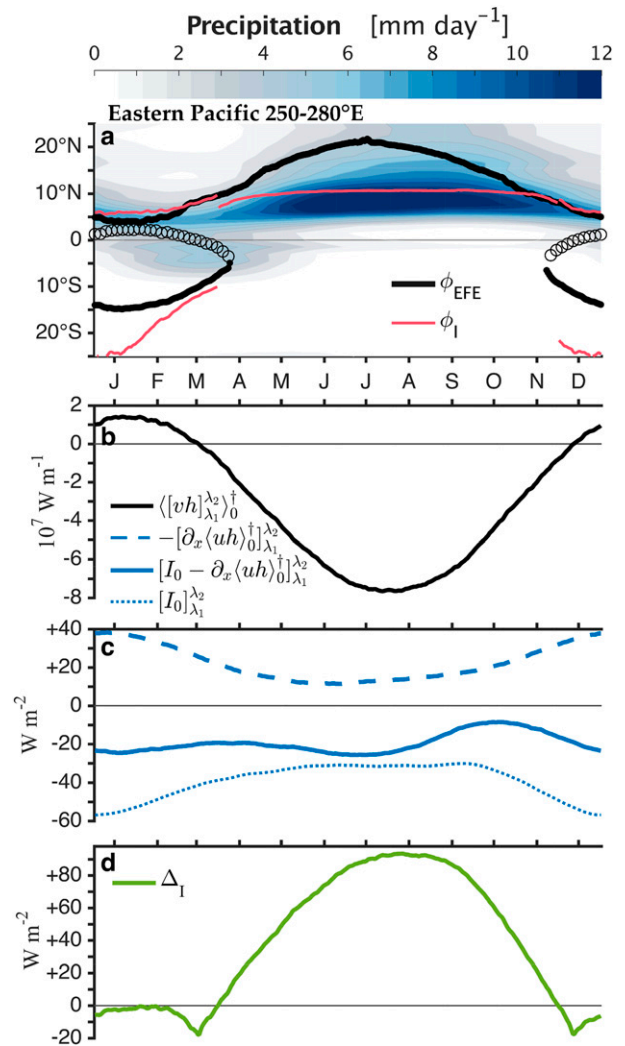


FIG. 7. (a) Daily climatology of zonal-mean precipitation (colors) in the eastern Pacific sector (250°–280°E). The EFE ϕ_{EFE} in the sector is shown as a thick black line. Convergent $\langle [vh]_{\lambda_1}^{\lambda_2} \rangle_0^{\dagger}$ zeros (implying a descending branch) are shown with open circles. The third-order approximations of the EFE [Eq. (8)] are shown in red. (b) Cross-equatorial divergent AET $\langle [vh]_{\lambda_1}^{\lambda_2} \rangle_0^{\dagger}$. (c) Local NEI (solid blue), composed of zonal net energy input $-\partial_x \langle [uh]_{\lambda_1}^{\lambda_2} \rangle_0^{\dagger}$ (dashed blue), and vertical (TOA and surface) net energy input $[I_0]_{\lambda_1}^{\lambda_2}$ (dotted blue). (d) Discriminant Δ_I [Eq. (7)]. Cross-equatorial AET and equatorial derivatives are meridionally averaged between 5°S and 5°N. Data are taken from ERAI for 1979–2014 and are smoothed using a 91-day running mean.

The daily climatology of the eastern Pacific sector is shown in Fig. 7, with the third-order approximation [Eq. (8)] shown in red [Eq. (8a) for $\Delta_I > 0$ and Eq. (8b) for $\Delta_I < 0$]. The third-order approximation captures the EFE only qualitatively, with an increasing error the farther the EFE is from the equator. The bifurcation from a single- to double-ITCZ state in the eastern Pacific (Fig. 7a) lags the bifurcation in the EFE by about

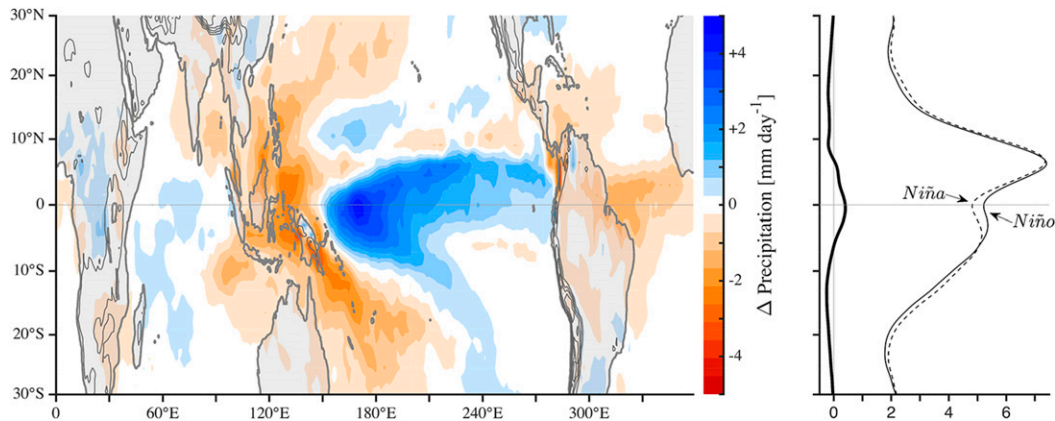


FIG. 8. (left) Precipitation difference between typical annual-mean El Niño and La Niña conditions. Orography is shown by gray contours at 1-km intervals. (right) The zonal mean of the precipitation difference (thick solid) and typical El Niño (thin solid) and La Niña (dashed) conditions. Typical El Niño (La Niña) conditions are defined as ONI values above 0.2 K (below -0.2 K). Data are taken from ERSST.v3b and ERAI for 1979–2014.

1–2 months. Similarly, as in the other sector means, the correlation between the seasonal variations of the northern EFE and ITCZ position is maximal for precipitation that lags EFE variations by about 1 month, as was the case for the zonal mean (Adam et al. 2016). The (lag corrected) EFE deviates from the ITCZ position by up to 10° latitude during boreal summer and in the southern branch of the boreal spring double ITCZ. Consistent with theory, a double-ITCZ state exists for $\Delta_I < 0$ (Fig. 7d; with a lag of 1–2 months) during boreal spring because of increased ocean heat uptake (i.e., reduced NEI) and vanishing cross-equatorial AET. The local NEI (solid blue) is the sum of the vertical (I_0 , dotted blue, negative year-round) and zonal ($-\partial_x(uh)_0^\dagger$, dashed blue, positive year-round) NEI. The seasonal bifurcation of the ITCZ in the eastern Pacific therefore depends on a complex balance between the vertical and zonal NEI components, which are themselves coupled via ocean–atmosphere interactions.

c. EFE response to ENSO

The zonal-mean precipitation tends to increase near the equator during El Niño episodes (e.g., Dai and Wigley 2000; Adam et al. 2016), which are characterized by sea surface temperature (SST) anomalies in the equatorial Pacific. Figure 8 shows the difference in the annual-mean precipitation between typical El Niño and La Niña conditions. Like the SST anomalies, the precipitation anomaly is most pronounced over the Pacific. In the zonal mean, precipitation maxima on either side of the equator shift equatorward (poleward) in response to warm (cold) El Niño (La Niña) episodes (Adam et al. 2016).

Figure 9 shows the annual-mean EFE during typical El Niño (magenta) and La Niña (green) conditions. Additionally, it shows the difference (El Niño minus La Niña) in the meridional component of the divergent AET $\langle v\bar{h} \rangle^\dagger$ (Fig. 9a) and in vertical (Fig. 9b) and zonal (Fig. 9c) NEI. We examine the annual-mean response in order to reduce the sensitivity of the analysis to ITCZ bifurcations, which are most frequent during boreal spring (e.g., Haffke et al. 2016). Like the ITCZ (Fig. 8), ENSO-related shifts in the EFE are most pronounced in the Pacific sector. During both El Niño and La Niña conditions, the EFE is south of the equator in the western Pacific and north of it in the central and eastern Pacific. However, the Pacific EFE lies significantly closer to the equator during El Niño conditions. ENSO-related variations in cross-equatorial AET (Fig. 9a) and zonal NEI (Fig. 9c) in the Pacific are relatively small. The equatorward shift of the EFE in the Pacific sector during El Niño episodes is therefore driven by increased NEI (Fig. 9b) because of the decreased ocean heat uptake (Schneider et al. 2014; Adam et al. 2016). Thus, the equatorward (poleward) shift of zonal-mean precipitation maxima on either side of the equator during El Niño (La Niña) episodes (Fig. 8) is consistent with the shifts of the EFE in the Pacific, which are primarily driven by variations in ocean heat uptake (Adam et al. 2016). However, like for bifurcations from single- to double-ITCZ states, variations in ocean heat uptake are themselves coupled to the atmospheric circulation and clouds. Therefore, a complete understanding of EFE and ITCZ variations associated with ENSO requires an understanding of the ocean–atmosphere coupling in the Pacific region.

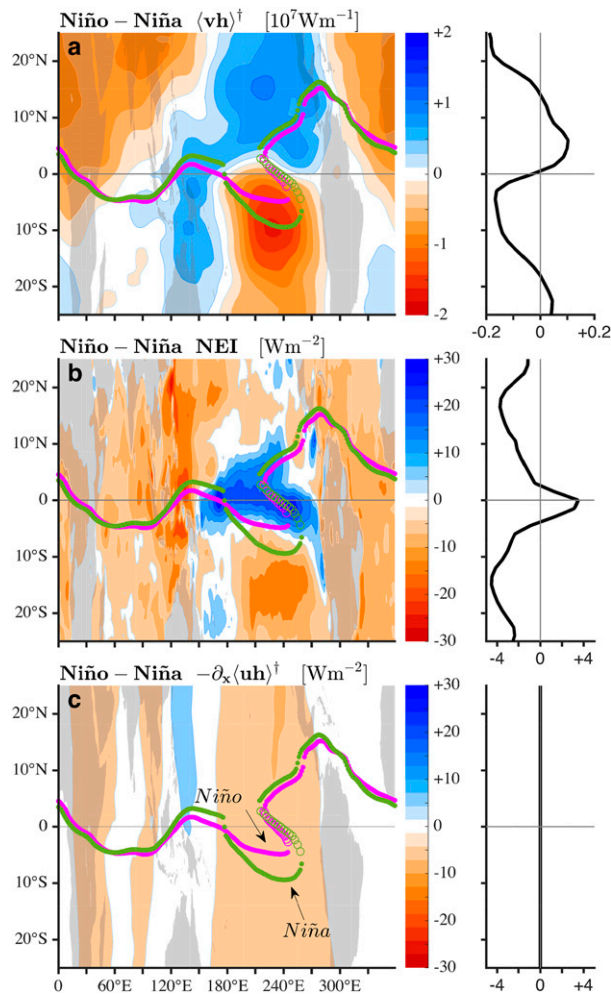


FIG. 9. (left) Difference between typical annual-mean El Niño and La Niña conditions of (a) the meridional component of the divergent MSE flux $\langle v h \rangle^\dagger$, (b) vertical (TOA and surface) net energy input I , and (c) zonal net energy input $-\partial_x \langle u h \rangle^\dagger$. The EFEs of typical El Niño and La Niña conditions are shown by magenta and green dots, respectively. Convergent zeros of $\langle v h \rangle^\dagger$ are shown with open circles and (right) the zonal means. Typical El Niño (La Niña) conditions are defined as ONI values above 0.2 (below -0.2). Data are taken from ERSST.v3b and ERAI for 1979–2014.

5. Summary and discussion

The ITCZ lies at the ascending branch of the tropical meridional overturning circulation, where near-surface mass fluxes vanish. The ITCZ position (identified as the precipitation maximum) is also located near the atmospheric EFE, where column-integrated energy fluxes diverge and vanish. Since the EFE is characterized by meridional divergence of the column-integrated atmospheric energy transport, the zonally varying EFE is found as the latitude where the meridional component of the divergent AET both vanishes and has a positive meridional gradient.

Like the ITCZ, the zonally varying EFE migrates seasonally toward the differentially warming hemisphere. Its migrations capture some aspects of regional ITCZ migrations (Fig. 3). But at some longitudes, large discrepancies exist between the ITCZ position and EFE. Moreover, in the Pacific sector, the Walker circulation is of comparable magnitude to the meridional overturning circulation, making the correspondence between the EFE and ITCZ weak (in particular over the western Pacific, where the rising branch of the Walker circulation is located). Thus, discrepancies between the column-integrated energy and mass-flux equators, as well as the requirement that the circulation is primarily meridional, limit the applicability of the theory in some regions. However, outside the western Pacific, we find that sector-mean EFE variations capture key features of ITCZ position variations.

The EFE and roughly the ITCZ position can be approximated by meridionally expanding the divergent component of the AET around the equator (Bischoff and Schneider 2014). To a first order, the ITCZ position is proportional to the divergent cross-equatorial AET and inversely proportional to the local NEI, which is the net of vertical fluxes across the surface and top of the atmosphere, and zonal fluxes across sector boundaries. The first-order approximation captures the cross-equatorial monsoonal migrations of the ITCZ over the African and Asian sectors and the limited seasonal migrations north of the equator over the Atlantic sector (Fig. 5). In these regions, seasonal ITCZ migrations are associated with both cross-equatorial AET and local equatorial NEI variations. This is in contrast to the seasonal migrations of the zonal-mean ITCZ, which are dominated by cross-equatorial AET (Donohoe et al. 2013; Adam et al. 2016). Like the zonal-mean ITCZ (Adam et al. 2016), seasonal ITCZ migrations lag EFE variations by about 1 month, for reasons that are not clear.

Since the meridional derivative of the AET at the equator is negative in the Pacific sector (i.e., approximately local NEI; Fig. 4), third-order approximations are required there. A simplified third-order approximation [Eq. (8)] is obtained by assuming second derivatives of the AET are weak near the equator (because of the approximate antisymmetry of the AET about the equator). The third-order approximation captures the single-ITCZ phase [Eq. (8a), boreal summer to boreal autumn] and the bifurcation to a double ITCZ during boreal spring [Eq. (8b)] in the eastern Pacific (Fig. 8, left) only qualitatively; the discrepancy between the AET zeros and ITCZ branches can be as large as 10° latitude (Fig. 7a). Consistent with theory, the eastern Pacific ITCZ bifurcates from single to double ITCZ

when the discriminant Δ_I [Eq. (7)] is negative (Fig. 7; with a lag of 1–2 months). Likewise consistent with theory, observations indicate that a double ITCZ is more likely to occur during La Niña episodes (Zhang 2001; Gu et al. 2005). The latter observation supports the theory (Bischoff and Schneider 2016) because during cold La Niña episodes ocean heat uptake increases and NEI decreases (Fig. 9), while variations in cross-equatorial AET are negligible (Fig. 9); therefore, Δ_I is generally smaller.

Since local NEI is negative in the Pacific, the predictions of linear EFE theory, which relates the ITCZ position only to cross-equatorial AET (e.g., Kang et al. 2008, 2009; Donohoe et al. 2013, 2014), are invalid there. Contrary to linear EFE theory, for negative local NEI, the ITCZ latitude and cross-equatorial AET can have the same sign (Fig. 6a). Moreover, eastern Pacific ITCZ variability (which includes bifurcations from single- to double-ITCZ states during boreal spring) is driven by a complex balance between the vertical and zonal NEI components as well as variations in cross-equatorial AET.

Correlations of interannual variations in sector-mean EFE and ITCZ position were found to be statistically insignificant in the reanalysis data. However, since seasonal variations of the sector-mean EFE and ITCZ position are in qualitative agreement (Figs. 5 and 7), the low interannual correlations are likely due to weak interannual variations outside the Pacific (Fig. 9, assuming interannual variations are primarily ENSO driven; Adam et al. 2016) and the complex nature of ITCZ variability in the Pacific. In monsoonal regions, the EFE and ITCZ position were found to be collocated in simulations driven by a wide range of forcing scenarios (Shekhar and Boos 2016). The relevance of the theory in different regions over a wide range of simulated climates remains to be tested.

ENSO-related variations in the ITCZ (Fig. 8) and EFE (Fig. 9) are most pronounced in the Pacific. As in the zonal-mean case (Adam et al. 2016), these variations are characterized by an equatorward shift of the ITCZ and EFE during warm El Niño episodes and a poleward shift during La Niña episodes. These variations are driven by increased (decreased) NEI (Fig. 9b), because of decreased (increased) ocean heat uptake during El Niño (La Niña) episodes (Schneider et al. 2014; Adam et al. 2016). Paleorecords indicate that a similar contraction or expansion of the annual-mean tropical precipitation belt in the Pacific also occurs on decadal or longer time scales (e.g., Yan et al. 2015). Similarly, records indicate large local meridional shifts of the ITCZ in past climates (Schneider et al. 2014). Better understanding of the zonally varying atmospheric energy budgets of past climates may improve our understanding

of associated local and zonal-mean tropical precipitation patterns.

Acknowledgments. We thank Momme Hell for his visualization advice.

APPENDIX

Third-Order Approximation

The approximate zeros in Eq. (8) are derived here for the following polynomial:

$$F_0 + F_1\phi + F_2\phi^2 + F_3\phi^3, \quad (\text{A1})$$

where $F_0 = \langle \nu h \rangle^\dagger$, $F_1 = a\partial_y \langle \nu h \rangle^\dagger \simeq aI_\phi^*$, $F_2 = a^2\partial_{yy} \langle \nu h \rangle^\dagger/2$, and $F_3 = a^3\partial_{yyy} \langle \nu h \rangle^\dagger/6$. For a negligible F_2 , the polynomial has a single real solution for $\Delta_I > 0$ and three distinct real roots for $\Delta_I < 0$, where $a\Delta_I = F_1 + (6F_0^2F_3)^{1/3}$. For $\Delta_I > 0$, assuming the first- and second-order terms are weak [i.e., unlike for the zero in Eq. (6) for large positive NEI, the balance is not predominantly linear], the dominant balance is between the zeroth- and third-order terms. Thus, we find

$$\phi_I = \left(\frac{-F_0}{F_3} \right)^{1/3} = \frac{1}{a} \left(\frac{-6\langle \nu h \rangle_0^\dagger}{\partial_{yy} I_0^*} \right)^{1/3}. \quad (\text{A2})$$

For $\Delta_I < 0$, the three roots correspond to two ITCZ positions (where $\langle \nu h \rangle_0^\dagger = 0$ and $\partial \langle \nu h \rangle_0^\dagger > 0$) and to the divider between the ITCZs (where $\langle \nu h \rangle_0^\dagger = 0$ and $\partial \langle \nu h \rangle_0^\dagger < 0$). We seek solutions using a first-order asymptotic expansion in F_0 , such that

$$\phi_I = \phi_0 + \phi_1 F_0 + O(F_0^2). \quad (\text{A3})$$

We solve for ϕ_0 and ϕ_1 by inserting Eq. (A3) into Eq. (A1) and solving for the zeroth- and first-order terms in F_0 separately:

$$\phi_0 = 0, \frac{-F_2 \pm \sqrt{F_2^2 - 4F_3F_1}}{2F_3} \quad (\text{A4})$$

and

$$\phi_1 = -\frac{1}{F_1} (2F_1 + F_2\phi_0)^{-1}. \quad (\text{A5})$$

For a weak F_2 ,

$$\phi_0 \simeq -\frac{3}{2a} \frac{\partial_y I_0^*}{\partial_{yy} I_0^*} \pm \frac{1}{a} \sqrt{\frac{-6I_0^*}{\partial_{yy} I_0^*}}, \quad (\text{A6})$$

so that the two roots corresponding to the ITCZ positions are approximately given by

$$\phi_I = -\frac{3}{2a} \frac{\partial_y I_0^*}{\partial_{yy} I_0^*} \pm \frac{1}{a} \sqrt{\frac{-6I_0^*}{\partial_{yy} I_0^*}} + \frac{\langle vh \rangle_0^\dagger}{a} \left[2I_0^* + \frac{\partial_y I_0^*}{2} \left(-\frac{3}{2} \frac{\partial_y I_0^*}{\partial_{yy} I_0^*} \pm \sqrt{\frac{-6I_0^*}{\partial_{yy} I_0^*}} \right) \right]^{-1}. \quad (\text{A7})$$

Setting $\partial_y I_0^* = 0$ (i.e., $F_2 = 0$) in Eq. (A7) reproduces the solution presented in Bischoff and Schneider [2016, their Eq. (13)]. Note, however, that Eq. (13) in Bischoff and Schneider (2016) contains an error: the factor $1/3$ should be replaced with $1/2$ in the second rhs term. The divider ϕ_D is given by the same relation as the first-order approximation in Eq. (5b):

$$\phi_D = -\frac{1}{a} \frac{\langle vh \rangle_0^\dagger}{\partial_y \langle vh \rangle_0^\dagger} \simeq -\frac{1}{a} \frac{\langle vh \rangle_0^\dagger}{I_0^*}, \quad (\text{A8})$$

however, contrary to the first-order approximation we have $I_0^* < 0$, so ϕ_D has the same sign as $\langle vh \rangle_0^\dagger$.

REFERENCES

- Adam, O., T. Bischoff, and T. Schneider, 2016: Seasonal and interannual variations of the energy flux equator and ITCZ. Part I: Zonally averaged ITCZ position. *J. Climate*, **29**, 3219–3230, doi:10.1175/JCLI-D-15-0512.1.
- Back, L. E., and C. S. Bretherton, 2006: Geographic variability in the export of moist static energy and vertical motion profiles in the tropical Pacific. *Geophys. Res. Lett.*, **33**, L17810, doi:10.1029/2006GL026672.
- Bischoff, T., and T. Schneider, 2014: Energetic constraints on the position of the intertropical convergence zone. *J. Climate*, **27**, 4937–4951, doi:10.1175/JCLI-D-13-00650.1.
- , and —, 2016: The equatorial energy balance, ITCZ position, and double ITCZ bifurcations. *J. Climate*, **29**, 2997–3013, doi:10.1175/JCLI-D-15-0328.1.
- Broccoli, A. J., K. A. Dahl, and R. J. Stouffer, 2006: Response of the ITCZ to Northern Hemisphere cooling. *Geophys. Res. Lett.*, **33**, L01702, doi:10.1029/2005GL024546.
- Chiang, J. C. H., and C. M. Bitz, 2005: Influence of high latitude ice cover on the marine intertropical convergence zone. *Climate Dyn.*, **25**, 477–496, doi:10.1007/s00382-005-0040-5.
- , and A. R. Friedman, 2012: Extratropical cooling, interhemispheric thermal gradients, and tropical climate change. *Annu. Rev. Earth Planet. Sci.*, **40**, 383–412, doi:10.1146/annurev-earth-042711-105545.
- Dai, A., and T. M. L. Wigley, 2000: Global patterns of ENSO-induced precipitation. *Geophys. Res. Lett.*, **27**, 1283–1286, doi:10.1029/1999GL011140.
- Dee, D. P., and Coauthors, 2011: The ERA-Interim reanalysis: Configuration and performance of the data assimilation system. *Quart. J. Roy. Meteor. Soc.*, **137**, 553–597, doi:10.1002/qj.828.
- Donohoe, A., J. Marshall, D. Ferreira, and D. McGee, 2013: The relationship between ITCZ location and cross-equatorial atmospheric heat transport: From the seasonal cycle to the Last Glacial Maximum. *J. Climate*, **26**, 3597–3618, doi:10.1175/JCLI-D-12-00467.1.
- , —, —, K. Armour, and D. McGee, 2014: The interannual variability of tropical precipitation and interhemispheric energy transport. *J. Climate*, **27**, 3377–3392, doi:10.1175/JCLI-D-13-00499.1.
- Fasullo, J. T., and K. E. Trenberth, 2008: The annual cycle of the energy budget. Part II: Meridional structures and poleward transports. *J. Climate*, **21**, 2313–2325, doi:10.1175/2007JCLI1936.1.
- Frierson, D. M. W., and Y.-T. Hwang, 2012: Extratropical influence on ITCZ shifts in slab ocean simulations of global warming. *J. Climate*, **25**, 720–733, doi:10.1175/JCLI-D-11-00116.1.
- , and Coauthors, 2013: Contribution of ocean overturning circulation to tropical rainfall peak in the Northern Hemisphere. *Nat. Geosci.*, **6**, 940–944, doi:10.1038/ngeo1987.
- Gu, G., R. Adler, and A. Sobel, 2005: The eastern Pacific ITCZ during the boreal spring. *J. Atmos. Sci.*, **62**, 1157–1174, doi:10.1175/JAS3402.1.
- Haffke, C., G. Magnusdottir, D. Henke, P. Smyth, and Y. Peings, 2016: Daily states of the March–April east Pacific ITCZ in three decades of high-resolution satellite data. *J. Climate*, **29**, 2981–2995, doi:10.1175/JCLI-D-15-0224.1.
- Irving, R. S., 2004: *Integers, Polynomials, and Rings*. Springer, 289 pp.
- Kang, S. M., I. M. Held, D. M. W. Frierson, and M. Zhao, 2008: The response of the ITCZ to extratropical thermal forcing: Idealized slab-ocean experiments with a GCM. *J. Climate*, **21**, 3521–3532, doi:10.1175/2007JCLI2146.1.
- , D. M. W. Frierson, and I. M. Held, 2009: The tropical response to extratropical thermal forcing in an idealized GCM: The importance of radiative feedbacks and convective parameterization. *J. Atmos. Sci.*, **66**, 2812–2827, doi:10.1175/2009JAS2924.1.
- Liu, Z., D. Ostranga, W. Teng, and S. Kempler, 2012: Tropical Rainfall Measuring Mission (TRMM) precipitation data and services for research and applications. *Bull. Amer. Meteor. Soc.*, **93**, 1317–1325, doi:10.1175/BAMS-D-11-00152.1.
- Marshall, J., A. Donohoe, D. Ferreira, and D. McGee, 2014: The ocean's role in setting the mean position of the inter-tropical convergence zone. *Climate Dyn.*, **42**, 1967–1979, doi:10.1007/s00382-013-1767-z.
- Neelin, J. D., and I. M. Held, 1987: Modeling tropical convergence based on the moist static energy budget. *Mon. Wea. Rev.*, **115**, 3–12, doi:10.1175/1520-0493(1987)115<0003:MTCBOT>2.0.CO;2.
- Peixoto, J. P., and A. H. Oort, 1992: *Physics of Climate*. American Institute of Physics, 555 pp.
- Schneider, T., T. Bischoff, and G. H. Haug, 2014: Migrations and dynamics of the intertropical convergence zone. *Nature*, **513**, 45–53, doi:10.1038/nature13636.
- Shekhar, R., and W. R. Boos, 2016: Improving energy-based estimates of monsoon location in the presence of proximal deserts. *J. Climate*, **29**, 4741–4761, doi:10.1175/JCLI-D-15-0747.1.
- Smith, T., R. Reynolds, T. Peterson, and J. Lawrimore, 2008: Improvements to NOAA's historical merged land–ocean surface temperature analysis (1880–2006). *J. Climate*, **21**, 2283–2296, doi:10.1175/2007JCLI2100.1.
- Trenberth, K. E., 1997: Using atmospheric budgets as a constraint on surface fluxes. *J. Climate*, **10**, 2796–2809, doi:10.1175/1520-0442(1997)010<2796:UABAAC>2.0.CO;2.
- , J. M. Caron, and D. P. Stepaniak, 2001: The atmospheric energy budget and implications for surface fluxes and ocean

- heat transports. *Climate Dyn.*, **17**, 259–276, doi:[10.1007/PL00007927](https://doi.org/10.1007/PL00007927).
- Voigt, A., and T. A. Shaw, 2015: Circulation response to warming shaped by radiative changes of clouds and water vapour. *Nat. Geosci.*, **8**, 102–106, doi:[10.1038/ngeo2345](https://doi.org/10.1038/ngeo2345).
- Yan, H., W. Wei, W. Soon, A. Zhisteng, W. Zhou, Z. Liu, Y. Wang, and R. Carter, 2015: Dynamics of the intertropical convergence zone over the western Pacific during the Little Ice Age. *Nat. Geosci.*, **8**, 315–320, doi:[10.1038/ngeo2375](https://doi.org/10.1038/ngeo2375).
- Yoshimori, M., and A. J. Broccoli, 2008: Equilibrium response of an atmosphere–mixed layer ocean model to different radiative forcing agents: Global and zonal mean response. *J. Climate*, **21**, 4399–4423, doi:[10.1175/2008JCLI2172.1](https://doi.org/10.1175/2008JCLI2172.1).
- Yu, J.-Y., C. Chou, and J. D. Neelin, 1998: Estimating the gross moist stability of the tropical atmosphere. *J. Atmos. Sci.*, **55**, 1354–1372, doi:[10.1175/1520-0469\(1998\)055<1354:ETGMSSO>2.0.CO;2](https://doi.org/10.1175/1520-0469(1998)055<1354:ETGMSSO>2.0.CO;2).
- Zhang, C., 2001: Double ITCZs. *J. Geophys. Res.*, **106**, 11 785–11 792, doi:[10.1029/2001JD900046](https://doi.org/10.1029/2001JD900046).